

Article

Tidal Flat Erosion Processes and Their Dynamic Mechanisms on the South Side of Sheyang River Estuary, Jiangsu Province

Wangze Zhang ^{1,2} , Kai Ouyang ^{3,*}, Xiaofei Zhang ^{3,4}, Aijun Wang ^{2,4,5,*} , Qian Yu ⁶ , Xiang Ye ² and Caihua Yao ³

¹ School of Advanced Manufacturing, Fuzhou University, Quanzhou 362251, China; zhangwangze111@163.com

² Laboratory of Coastal and Marine Geology, Third Institute of Oceanography, Ministry of Natural Resources, Xiamen 361005, China; yexiang@tio.org.cn

³ Institute of Geochemical Exploration and Marine Geological Survey, Nanjing 210007, China; we537@163.com (X.Z.); beyond-92@126.com (C.Y.)

⁴ Observation and Research Station of East China Coastal Zone, Ministry of Natural Resources, Nanjing 210001, China

⁵ Fujian Provincial Key Laboratory of Marine Physical and Geological Processes, Xiamen 361005, China

⁶ Ministry of Education Key Laboratory for Coast and Island Development, Nanjing University, Nanjing 210023, China; qianyu.nju@gmail.com

* Correspondence: 13585178813@126.com (K.O.); wangajun@tio.org.cn (A.W.)

Abstract: Tidal flats are accumulations of fine-grained sediment formed under the action of tides and play a very important role in coastal protection. The northern part of Jiangsu coast, as a typical example of muddy coasts found all over the world, has experienced serious erosion since the Yellow River shifted northward, and the range of erosion has been gradually extending southward, now reaching the south of the Sheyang River estuary (SYRE). In order to address coastal erosion near the SYRE through protective measures, there is an urgent need for research on the spatial and temporal variation of coastal erosion processes and their control mechanisms in the SYRE and adjacent coastal areas. For this study, the tidal flats on the south side of the SYRE were selected as the study area, and the sediment dynamics in the upper and lower intertidal flat were observed in different seasons to investigate the erosion processes and their dynamic mechanisms. The results show that the tidal current and wave action in the observed intertidal flats are stronger in winter than in summer, and these intertidal flats erode under the combined action of waves and currents. During winter, the net transport of the near-bottom suspended sediment and bedload is primarily towards the southeast, while in summer, the direction tends toward the north and northeast. The net transport fluxes are larger in the lower part of the intertidal flat than in the upper part in summer and also larger in winter than in summer within the lower intertidal flat. Furthermore, the tidal flat erosion in the study area manifests as shoreline retreat and flat surface erosion. The average shoreline retreat rate increased from 23.3 m/a during 2014–2019 to 43.5 m/a during 2019–2021, and the average erosion depth of the lower and upper parts of the intertidal flat over a tidal cycle is, respectively, 1.98 cm and 0.24 cm in winter and 1.65 cm and 0.26 cm in summer. The ratio of the wave-induced bottom shear stress to the tidal current-induced bottom shear stress is 0.40~0.46 in the lower intertidal flat and increases to 0.66~0.67 in the upper intertidal flat, indicating that the intertidal flat erosion in the study area is primarily driven by tidal currents, with significant contributions from wave action, especially in the upper intertidal flat.



Citation: Zhang, W.; Ouyang, K.; Zhang, X.; Wang, A.; Yu, Q.; Ye, X.; Yao, C. Tidal Flat Erosion Processes and Their Dynamic Mechanisms on the South Side of Sheyang River Estuary, Jiangsu Province. *J. Mar. Sci. Eng.* **2024**, *12*, 687. <https://doi.org/10.3390/jmse12040687>

Academic Editor: Markes E. Johnson

Received: 10 March 2024

Revised: 10 April 2024

Accepted: 16 April 2024

Published: 22 April 2024



Copyright: © 2024 by the authors. Licensee MDPI, Basel, Switzerland. This article is an open access article distributed under the terms and conditions of the Creative Commons Attribution (CC BY) license (<https://creativecommons.org/licenses/by/4.0/>).

Keywords: tidal flat; coastal erosion; sediment transport; wave action; Sheyang River estuary

1. Introduction

Tidal flats, formed under the significant influence of tidal action and rich conditions of fine-grained sediment supply, represent a distinct geomorphic feature situated at the interface of land, ocean, and atmosphere [1]. They exhibit significant spatial differences influenced by factors such as tidal range, waves, material supply, and vegetation cover [2].

Currently, the area corresponding to global tidal flats is approximately 127,921 km², mainly distributed in the Asia-Pacific region, such as in Indonesia, China, India, and other countries [3]. There has been substantial and systematic research on tidal flat sedimentation in the world, particularly along the North Sea coasts of European countries such as The Netherlands, Germany, and Denmark [4], the Wash Bay in the United Kingdom [5], Fundy Bay in Canada [6], and the Jiangsu tidal flats in China [7,8]. As an important part of the coastal zone, tidal flats play a crucial role in coastal protection [9]. However, due to sea-level rise, land subsidence, and intensive human activities in river basins and coastal zones, there has been a gradual decrease in the area of tidal flats globally [10,11], and most muddy coasts have suffered erosion [12,13].

The tidal flats in Jiangsu coast are famous for both rapid accretion and intense erosion. After the Yellow River shifted northward in 1855, the supply of huge amounts of sediment was cut off, resulting in erosion in the abandoned Yellow River delta (AYRD) and adjacent coast area, and the intensity of erosion gradually decreases with the increasing distance away from the AYRD center [8,14]. The coastal area south of the Sheyang River estuary (SYRE) (Figure 1a) exhibits signs of continuous accretion in the early stage, due to the transport of eroded sediment from the AYRD to the south [15–17]. However, since 2000, the coastal area south of the SYRE has also begun to gradually erode, and the intensity of this erosion has been gradually increasing [18–22]. Severe coastal erosion has severely impacted local socioeconomic development and damaged residents' property, necessitating ecological protection and restoration efforts. However, although there is a general understanding of the causes of coastal erosion [14,18–20], the spatial and temporal changes in coastal erosion on the coast near the Sheyang River estuary are complex; thus, there is insufficient understanding of the coastal erosion process and its spatiotemporal variations in this area, which seriously restricts the effectiveness of measures for coastal erosion protection and ecological restoration in the region. Generally speaking, the main methods for researching coastal erosion and accumulation mainly include (1) setting up fixed sections in typical areas for repeatedly monitoring profile elevation, which is analyzed to explore the dynamic change process of coastal erosion and accumulation [15,16]; (2) using time-series remote sensing images to study coastline changes [17,18]; (3) using remote sensing image interpretation or drone measurements to obtain data for the distribution of seabed elevation in different periods and analyzing the spatiotemporal variations in coastal erosion and accumulation [21]; (4) using in situ observation of hydrodynamics to calculate the erosion and accumulation processes and analyze their control mechanisms [22–24]; (5) using numerical modeling methods to carry out modeling research on tidal currents, waves, and sediment transport to simulate the evolution processes of coastal morphodynamics and their control mechanisms [25,26].

To obtain a clearer understanding of the processes of tidal flats erosion in Jiangsu coast, the tidal flats on the south side of the SYRE are selected as the study area, and the hydrodynamic and sediment transport processes and spatial pattern of tidal flat erosion near the SYRE and the surrounding coastal area are analyzed through in situ observation of the sediment dynamics. The dynamic mechanisms of tidal flat erosion are discussed toward establishing a scientific basis for coastal protection and ecological restoration near the SYRE.

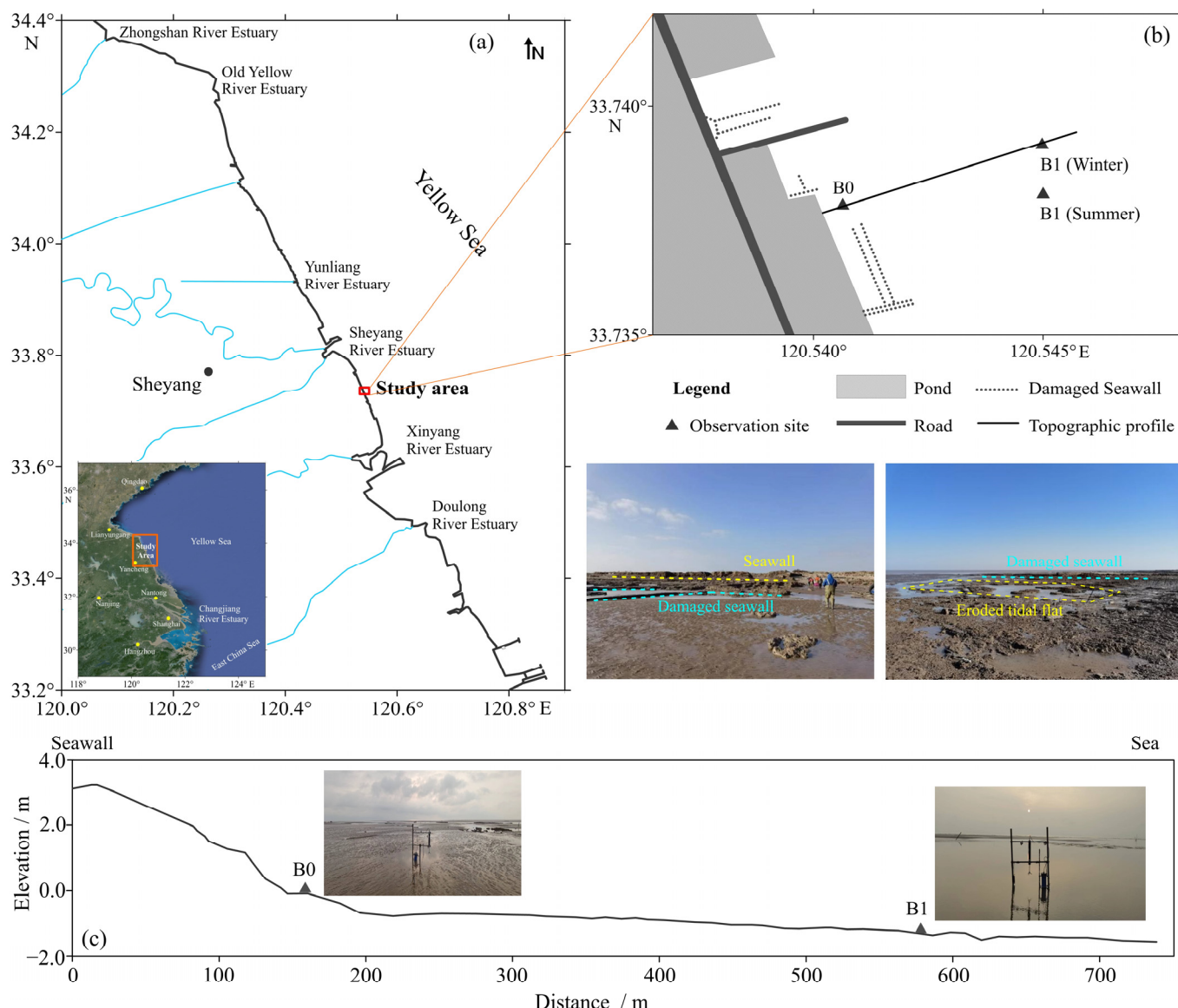


Figure 1. Sketch map of study area and observation sites: (a) location of study area; (b) observation sites; (c) profile of elevation indicating installation of on-site instruments.

2. Study Area

The Sheyang River estuary is located in the central part of the Jiangsu coast (Figure 1a). The average flood tide duration is 4 h 49 min and the average ebb tide duration is 7 h 36 min. The maximum tidal range is 4.16 m with a mean tidal range of 2.15 m, with irregular semi-diurnal tides and irregular tidal currents, which are mainly affected by the rotating tidal waves of the South Yellow Sea and the coastal current along the northern Jiangsu coast [27]. The intertidal geomorphology of the SYRE predominantly comprises tidal flats, which can be categorized into high-tide mud flats, mid-tide silt–mud mixed flats, and low-tide silt–fine sand flats. The area occupied by silt–mud tidal flats at mid- and high-tide levels is 56.20 km², while silt–fine sand tidal flats at low tide cover 84.73 km² [27].

As the southern end of the AYRD, the intensity and extent of coastal erosion at the Sheyang River mouth are continually expanding. Remote sensing monitoring results for the SYRE indicate that since the 1970s, the intensity of coastal erosion has decreased on the north side but gradually increased on the south side, particularly increasing since 2000 [17–19]. Field investigations have found that the coast south of the SYRE is seriously eroded, resulting in the destruction of many fishponds along the coast, and the safety

of roads and coastal projects is seriously threatened (Figure 1b). Due to the continuous intensification of coastal erosion, the region is gradually shifting from being a accretional muddy coast to an erosive sandy coast [27].

3. Methods

3.1. Field Observation

Due to monsoon control in the Jiangsu coastal area, there are significant differences in the dynamic environment between summer and winter, such as in terms of tidal currents and waves [8,26]. In order to deeply understand the seasonal variations in the dynamic conditions that cause tidal flat erosion, we conducted field observations in both winter and summer. Field observations of sediment dynamics were carried out on the intertidal flat on the south of the SYRE during 6–15 December 2021 and 10–18 June 2022, covering both winter and summer spring–neap tidal cycles (8 days). The key parameters observed included inundation height, tidal current velocity, flow direction, wave height, and suspended sediment concentration (SSC), and the observation sites are shown in Figure 1b. The acoustic Doppler velocimeter (ADV) (Nortek AS, Oslo, Norway) was used at each site. Data collection was set to burst mode, with a sampling interval of 30 min and a sampling frequency of 1 Hz during winter, with each sampling conducted for a duration of 1024 s. In order to obtain observation data with a higher time resolution, the sampling interval was set to 10 min and the sampling frequency was set to 4 Hz during summer, and each sampling duration to 256 s. After the instrument was installed, the height of the ADV probe from the flat surface was measured as 25 cm, and since the ADV measures the flow velocity at 15 cm from the instrument probe, the actual observed layer was at a height of 10 cm from the flat surface.

Surface sediments (0–1 cm) were collected at each site during low tide, sealed in plastic bags, and transported to the laboratory for analysis. After pretreatment of fully mixed sediment, including the removal of organic matter, carbonates, and dispersion, particle size analysis was conducted using a Mastersize2000 laser particle size analyzer (Malvern Panalytical Ltd., Malvern, UK) to determine the content and median grain size of surface sediments.

It should be noted that since the ADV probe is 25 cm above the seabed and the pressure sensor is 22 cm above the probe, accurate and complete hydrodynamic data were only recorded when the pressure sensor was submerged (i.e., inundation height > 47 cm). Therefore, “early flood tide” and “late ebb tide” refer to the moments when the pressure sensor was just submerged by the flood tide and emerged during ebb tide, respectively.

3.2. Calculation of Suspended Sediment Concentration

The data recorded by ADV include the signal–noise ratio (SNR), which is related to the suspended sediment concentration (SSC) in water. Therefore, it is possible to establish a relationship between SNR and SSC by conducting laboratory experiments, and the SNR signal recorded by ADV during in situ observations can then be converted to time-series SSC data; this method has been widely use in coastal areas [22,28,29]. Therefore, we prepared water samples with different SSCs in the laboratory to calibrate the ADV, and the water samples for each test were collected and filtered through preweighed 0.45 μm diameter filters. After filtration, the residue on the filters was washed with distilled water to remove sea salt. The washed filters were dried in an oven at 40 °C and then re-weighed using the same electronic balance to determine the SSC. Linear regression analysis was performed between the log(SSC) and corresponding SNR, as shown in Figure 2. Then, the relation between the SNR at each burst could be converted into the SSC.

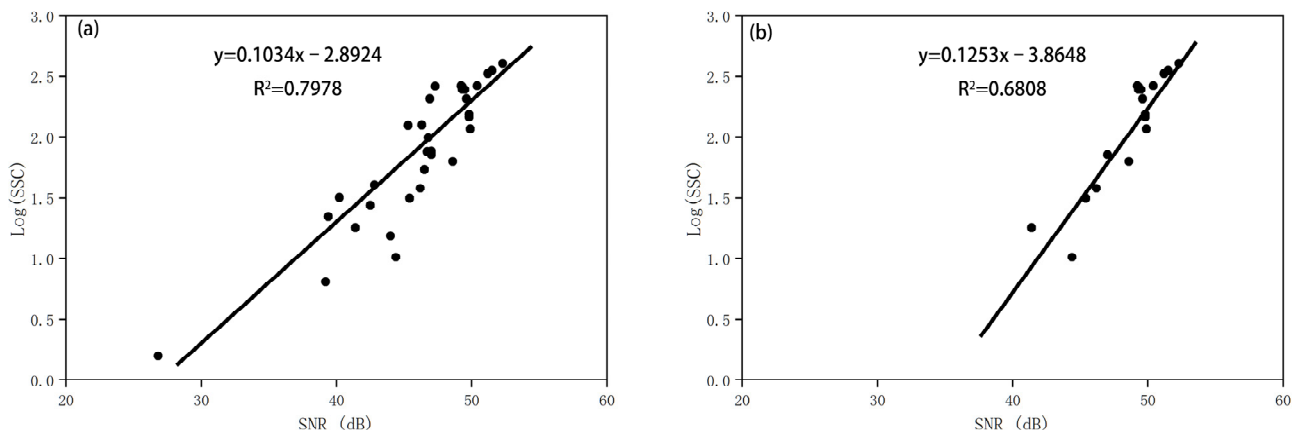


Figure 2. Relationship between SNR recorded by ADV and SSC ((a): B0 site; (b): B1 site).

3.3. Calculation of Sediment Dynamic Parameters

3.3.1. Calculation of Bottom Shear Stress

In intertidal regions, where water depth is shallow, the entire water column falls within the boundary layer range, and its velocity distribution conforms to a logarithmic profile [30]. Thus, the bottom shear stress induced by tidal currents can be computed using this method, which has been widely applied [31,32]. This assumes that the mean horizontal flow velocity profile within the boundary layer follows a logarithmic distribution and that the flow velocity decays with depth due to friction between the flow and the seabed. Then, the bottom shear stress induced by the tidal currents (τ_c) can be calculated and obtained using the following equation [31]:

$$U(z) = \frac{u_*}{k} \ln\left(\frac{z}{z_0}\right) \quad (1)$$

$$\tau_c = \rho_w u_*^2 \quad (2)$$

in which $U(z)$ is the mean horizontal flow velocity at height z from the seabed, u_* is the friction velocity, κ is the von Kármán constant ($\kappa = 0.4$), z_0 is the bed roughness, and ρ_w is the density of seawater ($\rho_w = 1025 \text{ kg/m}^3$). Considering the well-developed sand ripples near the observation site, z_0 is taken as $z_0 = 6 \text{ mm}$ in this paper according to the recommendation of Soulsby [33]. Since the ADV records pressure data at high frequencies, the significant wave height H_s can be calculated based on Longuet-Higgins [34]:

$$H_s = 4\sqrt{\int S_\eta(f) df} \quad (3)$$

where S_η is the power spectrum of the water level. When converting the pressure measured by ADV to water level, attenuation needs to be considered, and according to linear wave theory, the attenuation coefficient can be expressed as [35]

$$Kf = \frac{\cosh[k(z + h)]}{\cosh kh} \quad (4)$$

where k is the wave number, h is the mean water depth, and z is the depth of the pressure transducer (negative value). The wave-induced bottom shear stress (τ_w) can be calculated using the following equation [36]:

$$\tau_w = \frac{1}{2} \rho_w f_{wr} \hat{U}_\delta^2 \quad (5)$$

$$\hat{U}_\delta = \omega \hat{A}_\delta \quad (6)$$

$$\hat{A}_\delta = \frac{H_s}{2\sinh(\frac{2\pi}{L}h)} \quad (7)$$

where \hat{U}_δ is the wave orbital velocity at the edge of the wave boundary layer, ω is the angular velocity ($\omega = 2\pi/T$), \hat{A}_δ is the peak orbital offset, L is the wavelength, g is the gravitational acceleration (9.8 m/s^2), and T is the mean period. \hat{U}_δ can be accomplished by measuring $T_n = (h/g)^{1/2}$ directly from the input parameters H , T , h , and g [33].

The wave friction coefficient f_{wr} depends on the hydrodynamic state and can be expressed as [33]

$$f_{wr} = \begin{cases} 2Re_w^{-0.5}, & Re_w < 10^5 \text{ (Laminar)} \\ 0.0521Re_w^{-0.187}, & Re_w > 10^5 \text{ (Smooth turbulence)} \\ 0.237r^{-0.52}, & \text{(Rough turbulence)} \end{cases} \quad (8)$$

where Re_w is the wave Reynolds number, $r (= \hat{A}_\delta/k_s)$ is the relative roughness, k_s ($= 2.5d_{50}$) is the Nikuradse equivalent sediment grain roughness [33], and d_{50} is the median grain size of surface sediment. The bottom shear stress under the combined wave-current action (τ_{cw}) was calculated using the following equation [33]:

$$\tau_{cw} = \tau_c \left[1 + 1.2 \left(\frac{\tau_w}{\tau_c + \tau_w} \right)^{3.2} \right] \quad (9)$$

3.3.2. Calculation of Erosion and Deposition Fluxes

The deposition of suspended sediment and surface sediment erosion is determined by comparing the bottom shear stress (τ_b) with the critical shear stress for deposition (τ_{crd}) and the critical shear stress for erosion (τ_{cr}); if $\tau_b < \tau_{crd}$, suspended sediment in the water column occurs through deposition, and the seabed exhibits accretion, whereas if $\tau_b > \tau_{cr}$, resuspension of the surface sediment occurs, and the seabed experiences erosion. The following formulas for sediment erosion and deposition in coastal areas were used [37,38]:

$$F_E = m_e(\tau_b - \tau_{cr}), \tau_b > \tau_{cr} \quad (10)$$

$$F_D = \omega_s C \left(1 - \frac{\tau_b}{\tau_{crd}} \right), \tau_b < \tau_{crd} \quad (11)$$

where F_E is the erosion flux ($\text{kg/m}^2\cdot\text{s}$), m_e is the erosion constant ($\text{kg/m}^2\cdot\text{s}$), according to the grain size characteristics of the sediment in this study area and the recommendation of Robert and Whitehouse [39], $m_e = 0.002 \text{ kg/N}\cdot\text{s}$; F_D is the settling flux ($\text{kg/m}^2\cdot\text{s}$), C is the near-bed SSC (g/L), and we take the observed value of SSC at a height of 10 cm above the tidal flat surface. ω_s is the settling velocity of suspended sediment (m/s); τ_{crd} generally ranges between 0.06 and 0.1 N/m^2 . According to the recommendation of Robert and Whitehouse [39], $\tau_{crd} = 0.08 \text{ N/m}^2$ is taken in this paper.

Since the sediment in the study area is mainly composed of sand and silt, with minimal clay content, the τ_{cr} can be calculated using the following formulas [33]:

$$\theta_{cr} = \frac{\tau_{cr}}{g(\rho_s - \rho_w)d} \quad (12)$$

$$\theta_{cr} = \frac{0.30}{1 + 1.2D_*} + 0.055 \left(1 - e^{-0.020D_*} \right) \quad (13)$$

$$D_* = \left[\frac{g(s-1)}{\nu^2} \right]^{1/3} d \quad (14)$$

where θ_{cr} is the critical Shields parameter; ρ_s is the sediment density, which takes the value of $\rho_s = 2650 \text{ kg/m}^3$; d is the sediment grain size; D_* is a dimensionless parameter related to the sediment grain size; ν is the coefficient of dynamical viscosity of the water body, which takes the value of $1.36 \times 10^{-6} \text{ m}^2/\text{s}$; and $s = \rho_s/\rho_w$.

The settling velocity (ω_s) can be expressed as [40]

$$\omega_s = KC^m \quad (15)$$

where K and m are constants, which can be taken as $K = 0.00043$ and $m = 1.06$ based on experimental studies [40].

3.3.3. Calculation of Suspended Sediment and Bedload Transport

The instantaneous suspended sediment transport rate $f(t)$ and the net suspended sediment transport flux F_H during the tidal cycle at the observation layer can be calculated using the following formulas [40]:

$$f(t) = u(t)C(t) \quad (16)$$

$$F_H = \int_0^T f(t)dt = \sum_1^j \Delta t f_j(t) \quad (17)$$

where $C(t)$ represents the SSC in the observation layer at time t , $u(t)$ is the instantaneous velocity, and Δt represents the representative time length.

The bedload transport rate Q_b was calculated using the Bagnold method [33,41]:

$$Q_b = \rho_s q_b \quad (18)$$

$$q_b = \frac{0.1}{C_D^{1/2}(\tan \phi_i + \tan \beta)} \theta^{1/2} (\theta - \theta_{cr}) [g(s-1)d^3]^{1/2} \quad (19)$$

$$C_D = \left[\frac{0.40}{1 + \ln(z_0/h)} \right]^2 \quad (20)$$

in which q_b is the volume transport rate of the bedload; C_D is the drag coefficient; θ is the Shields parameter, which can be calculated according to Equation (12); ϕ is the angle of repose of the sediment, set to $\phi = 32^\circ$; and β is the slope of the tidal flat, which can be calculated based on field topographic profile observations.

4. Results

4.1. Surface Sediment Characters

The results of grain size analysis show that the surface sediments at the observation sites are dominated by silt and sand, with low clay content (Figure 3). The median grain size of the surface sediments at site B0 and B1 are 4.04Φ and 3.67Φ , respectively. Then, the critical shear stress for erosion can be calculated using Equations (12)–(14), and the results show that $\tau_{cr} = 0.118 \text{ N/m}^2$ at B0 and $\tau_{cr} = 0.131 \text{ N/m}^2$ at B1, respectively.

4.2. Hydrodynamic Characteristics

The observation results for winter (Figure 4, Table 1) show that the maximum inundation height at B1 and B0 decreased from 3.31 m and 1.69 m during spring tide to 2.58 m and 0.93 m during neap tide, respectively; the average near-bottom current velocities during the tidal cycle decreased from 0.288 m/s and 0.092 m/s during spring tides to 0.196 m/s and 0.064 m/s during neap tides, respectively. The tidal currents generally exhibit a southeast–northwest reciprocating flow. The maximum significant wave heights during the observation are 0.98 m (with a mean value of 0.39 m) with wave periods ranging from 2.6 s to 5.8 s (with a mean value of 3.8 s) at B1 and 0.72 m (with a mean value of 0.29 m) with wave periods ranging from 2.7 s to 6.1 s (with a mean value of 4.2 s) at B0. The calculated results indicate that the maximum values of τ_c at B1 and B0 are

3.392 N/m^2 and 1.174 N/m^2 , respectively, during spring tides and 0.606 N/m^2 and 0.123 N/m^2 , respectively, during neap tides, while the maximum values of τ_w are 0.751 N/m^2 and 0.361 N/m^2 , respectively, and the maximum values of τ_{cw} are 3.394 N/m^2 and 1.177 N/m^2 , respectively.

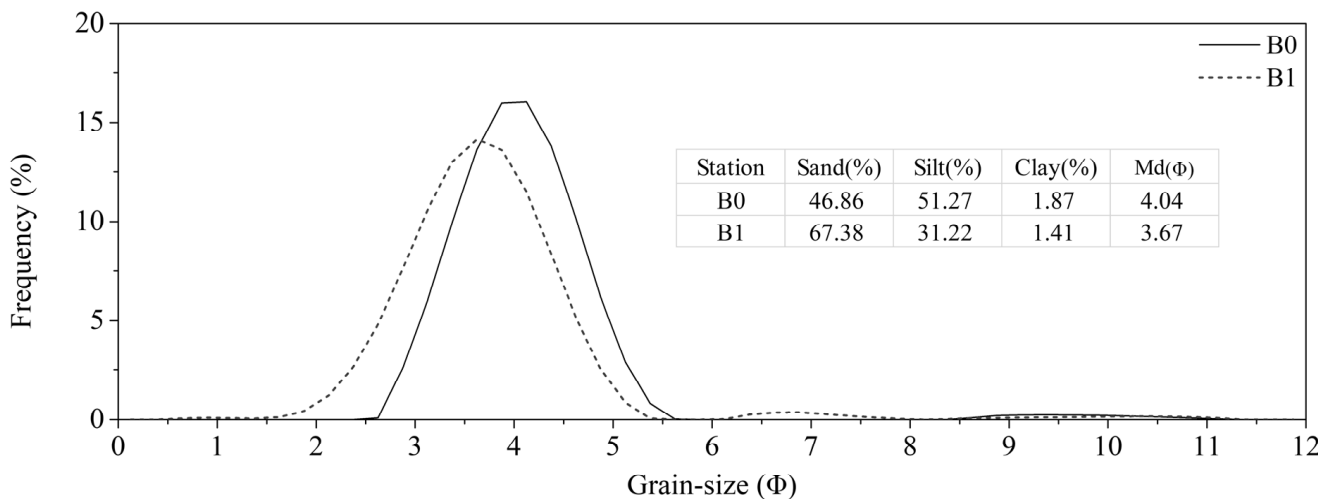


Figure 3. Grain size frequency curves of sediments in the upper and lower intertidal flats of the study area.

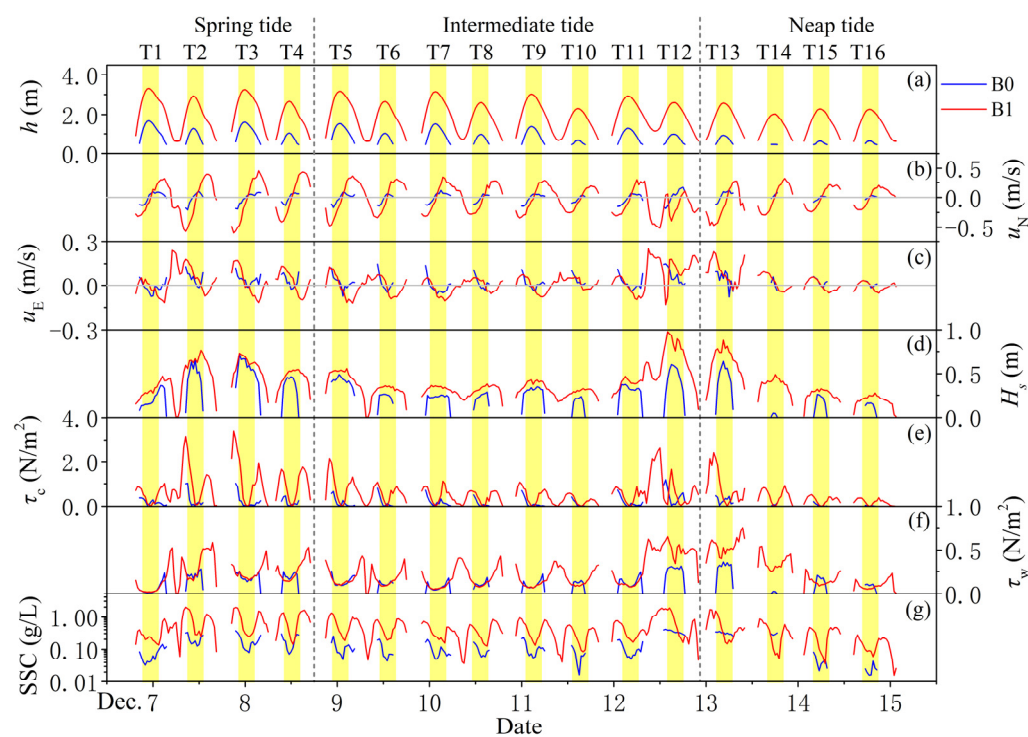


Figure 4. Near-bottom time-series sediment dynamics parameters in winter 2021 at sites B0 and B1: (a) inundation height; (b) near-bottom northward current velocity; (c) near-bottom eastward current velocity; (d) significant wave height; (e) bottom shear stress induced by tidal currents; (f) bottom shear stress induced by waves; and (g) near-bottom SSC. The red curve is the data from B1 in the lower intertidal flat, and the blue curve is the data from B0 in the upper intertidal flat. The yellow bands represent the number of tidal cycles.

Table 1. Statistical values of observed and calculated sediment dynamic parameters.

Station	Season	Statistical Value	<i>h</i> (m)	<i>H_s</i> (m)	<i>T</i> (s)	<i>u_a</i> (m/s)	SSC (g/L)	τ_c (N/m ²)	τ_w (N/m ²)	τ_{cw} (N/m ²)
B0	Winter	Maximum	1.690	0.716	6.130	0.238	0.412	1.174	0.361	1.177
		Mean	0.877	0.294	4.181	0.083	0.145	0.196	0.132	0.211
		Deviation	0.356	0.177	0.630	0.052	0.103	0.237	0.091	0.234
	Summer	Maximum	2.130	0.677	5.897	0.302	0.469	0.980	0.287	0.980
		Mean	1.224	0.312	4.049	0.120	0.136	0.197	0.091	0.205
		Deviation	0.393	0.148	0.572	0.063	0.103	0.186	0.062	0.184
B1	Winter	Maximum	3.313	0.979	5.757	0.621	1.968	3.392	0.751	3.394
		Mean	1.860	0.389	3.800	0.232	0.507	0.606	0.243	0.627
		Deviation	0.747	0.183	0.497	0.123	0.428	0.604	0.168	0.599
	Summer	Maximum	3.725	0.856	6.047	0.394	2.400	1.662	0.550	1.665
		Mean	2.123	0.378	3.877	0.196	0.589	0.495	0.195	0.509
		Deviation	0.868	0.142	0.571	0.089	0.417	0.360	0.117	0.356

Notes: *h*: inundation height, *H_s*: significant wave height, *T*: wave period, *u_a*: mean horizontal current velocity, SSC: suspended sediment concentration. τ_c , τ_w , and τ_{cw} represents bottom shear stress induced by tidal currents, waves, and the combined action of waves and currents, respectively.

The results for summer indicate that the variations in inundation height and near-bottom tidal current velocity between neap tides and spring tides were not significant (Figure 5, Table 1), and the tidal current also shows a southeast–northwest reciprocating flow. The maximum significant wave heights during the observation in summer are 0.86 m (with a mean value of 0.38 m) with wave periods ranging from 2.9 s to 6.9 s (with a mean value of 3.9 s) at B1 and 0.68 m (with a mean value of 0.31 m) with wave periods ranging from 2.0 s to 5.9 s (with a mean value of 4.0 s) at B0. The calculated results indicate that the maximum values of τ_c at B1 and B0 are 1.662 N/m² and 0.980 N/m², respectively, during the observation in summer and 0.550 N/m² and 0.287 N/m² for τ_w , respectively, while the maximum values of τ_{cw} are 1.665 N/m² and 0.980 N/m², respectively.

4.3. Suspended Sediment Concentration

The results calculated for SSC (Figures 4g and 5g, Table 1) reveal that the maximum values of the near-bed SSC at B1 and B0 were 1.968 g/L and 0.412 g/L, respectively, in winter and 2.400 g/L and 0.469 g/L in summer, respectively, and the SSC was significantly larger in the lower intertidal flat than in the upper intertidal flat. The near-bed SSC in the study area is characterized by obvious temporal variations: (1) Within the tidal cycle, the maximum SSC occurs at the early stage of the flood tide, and there is a gradual decrease with the increase in immersion time and inundation height, followed by a slow increase after high tide and reaching a higher value of SSC in the later stage of ebb tide, with the concentration greater during flood tide than that during ebb tide. (2) At the scale of spring–neap tide, the average SSC at B1 decreases from 0.706 g/L during spring tides to 0.350 g/L during neap tides in winter, with little variation at B0, while there is no obvious difference in SSC between spring and neap tides at the two sites in summer. (3) At the seasonal scale, the average SSC at B1 and B0 are 0.507 g/L and 0.145 g/L, respectively, in winter, while those in summer are 0.589 g/L and 0.136 g/L, respectively.

4.4. Erosion–Sedimentation Fluxes

The results calculated for bottom shear stress indicate that τ_c and τ_w at B1 and B0 are mostly greater than τ_{cr} in both winter and summer (Figures 4 and 5), indicating that the tidal flat in the study area experiences erosion most of the time. The results calculated for F_E and F_D reveal that the intertidal flat in the study area was mainly eroded during the observation, and the instantaneous erosion fluxes caused by τ_{cw} at B1 and B0 had maximum values of -6.53×10^{-3} kg/m²·s and -2.12×10^{-3} kg/m²·s, respectively, in the winter and -3.07×10^{-3} kg/m²·s and -1.72×10^{-3} kg/m²·s in the summer, respectively. The

statistical results show that the maximum total erosion fluxes within a tidal cycle at B1 and B0 were -77.68 kg/m^2 and -15.64 kg/m^2 , respectively, in winter and -45.51 kg/m^2 and -11.88 kg/m^2 in summer, respectively, while the maximum deposition fluxes of suspended sediment were only 0.10 kg/m^2 and 0.07 kg/m^2 , respectively, in winter and 0.86 kg/m^2 and 0.06 kg/m in summer, respectively (Figure 6, Table 2). The study area exhibits net erosion both in winter and summer, with net erosion fluxes of -622.31 kg/m and -516.50 kg/m^2 , respectively, at B1 and -75.37 kg/m^2 and -83.00 kg/m^2 at B0, respectively. The erosion of the intertidal flat has distinctive spatiotemporal variation characteristics, i.e., the erosion and deposition fluxes are larger in the lower than in the upper intertidal flat, and the erosion fluxes in the lower intertidal flat are larger in winter than in summer, while those in the upper intertidal flat exhibit the opposite pattern.

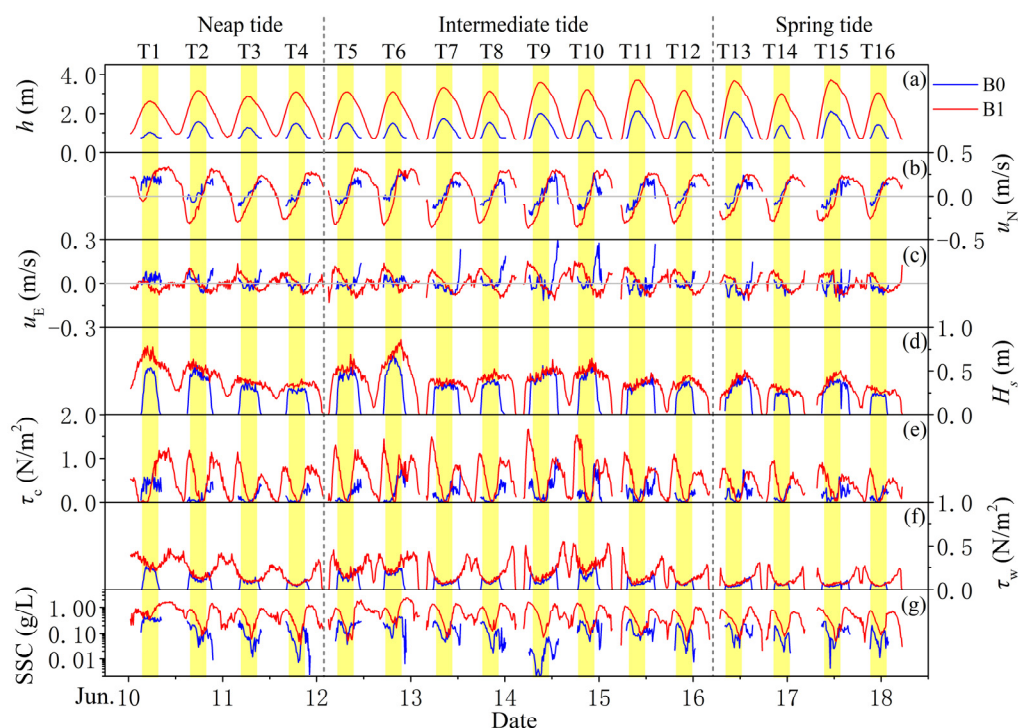


Figure 5. Near-bottom time-series sediment dynamics parameters in summer 2022 at sites B0 and B1: (a) inundation height; (b) near-bottom northward current velocity; (c) near-bottom eastward current velocity; (d) significant wave height; (e) bottom shear stress induced by tidal currents; (f) bottom shear stress induced by waves; and (g) near-bottom SSC. The red curve is the data from B1 in the lower intertidal flat, and the blue curve is the data from B0 in the upper intertidal flat. The yellow bands represent the number of tidal cycles.

4.5. Suspended Sediment and Bedload Transport Fluxes

The calculated results show that the net transport fluxes of near-bottom suspended sediment within the tidal cycle at B1 and B0 range from 72.9 kg/m to $10,167.6 \text{ kg/m}$ and from 2.8 kg/m to 539.4 kg/m , respectively, in winter and from 74.6 kg/m to 9455.7 kg/m and from 13.6 kg/m to 1237.2 kg/m in summer, respectively (Figure 7). The maximum bedload transport rate caused by τ_{cw} at B1 and B0 are $5.78 \times 10^{-2} \text{ kg/m}\cdot\text{s}$ and $0.79 \times 10^{-2} \text{ kg/m}\cdot\text{s}$, respectively, in winter and $1.94 \times 10^{-2} \text{ kg/m}\cdot\text{s}$ and $0.65 \times 10^{-2} \text{ kg/m}\cdot\text{s}$ in summer, respectively. The statistical results show that the net bedload transport fluxes within the tidal cycle at B1 and B0 range from 3.12 kg/m to 331.60 kg/m and from 0 to 28.25 kg/m , respectively, in winter and from 1.95 kg/m to 191.98 kg/m and from 1.24 kg/m to 30.44 kg/m in summer, respectively (Figure 8).

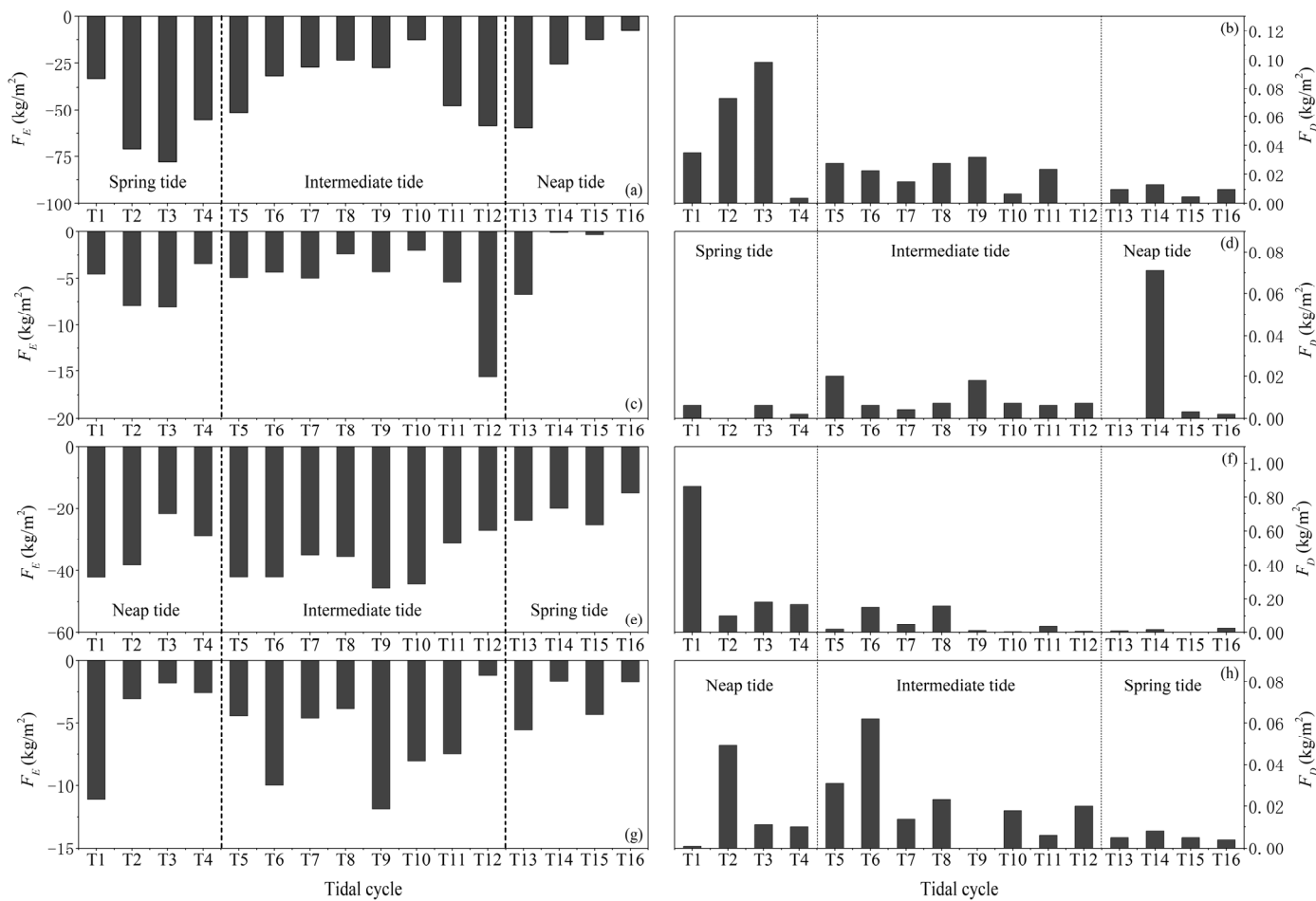


Figure 6. Total erosion–deposition fluxes within a tidal cycle during the observation period in the study area: (a) erosion and (b) deposition fluxes at B1 in winter; (c) erosion and (d) deposition fluxes at B0 in winter; (e) erosion and (f) deposition fluxes at B1 in summer; (g) erosion and (h) deposition fluxes at B0 in summer.

Table 2. Erosion and deposition rates within a tidal cycle.

Station	Season	Statistical Value	Erosion Rate ($\times 10^{-3} \text{ kg/m}^2 \cdot \text{s}$)			Deposition Rate ($\times 10^{-5} \text{ kg/m}^2 \cdot \text{s}$)		
			F_{E-c}	F_{E-w}	F_{E-cw}	F_{D-c}	F_{D-w}	F_{D-cw}
B0	Winter	Maximum	-2.111	-0.486	-2.118	2.848	6.136	2.840
		Mean	-0.505	-0.176	-0.494	0.233	0.864	0.148
	Summer	Maximum	-1.724	-0.338	-1.724	2.625	7.043	2.624
		Mean	-0.404	-0.107	-0.400	0.288	0.388	0.213
B1	Winter	Maximum	-6.522	-1.239	-6.525	6.832	18.070	3.959
		Mean	-1.220	-0.383	-1.205	0.718	1.025	0.594
	Summer	Maximum	-3.061	-0.837	-3.069	21.721	9.565	17.338
		Mean	-0.959	-0.269	-0.959	2.536	1.179	2.079

Notes: $FE-c$, $FE-w$, and $FE-cw$ are erosion rates induced by tidal currents, waves, and the combined action of waves and currents, respectively; $FD-c$, $FD-w$, and $FD-cw$ are deposition rates induced by tidal currents, waves, and the combined action of waves and currents, respectively. A negative value represents erosion, and a positive value represents deposition.

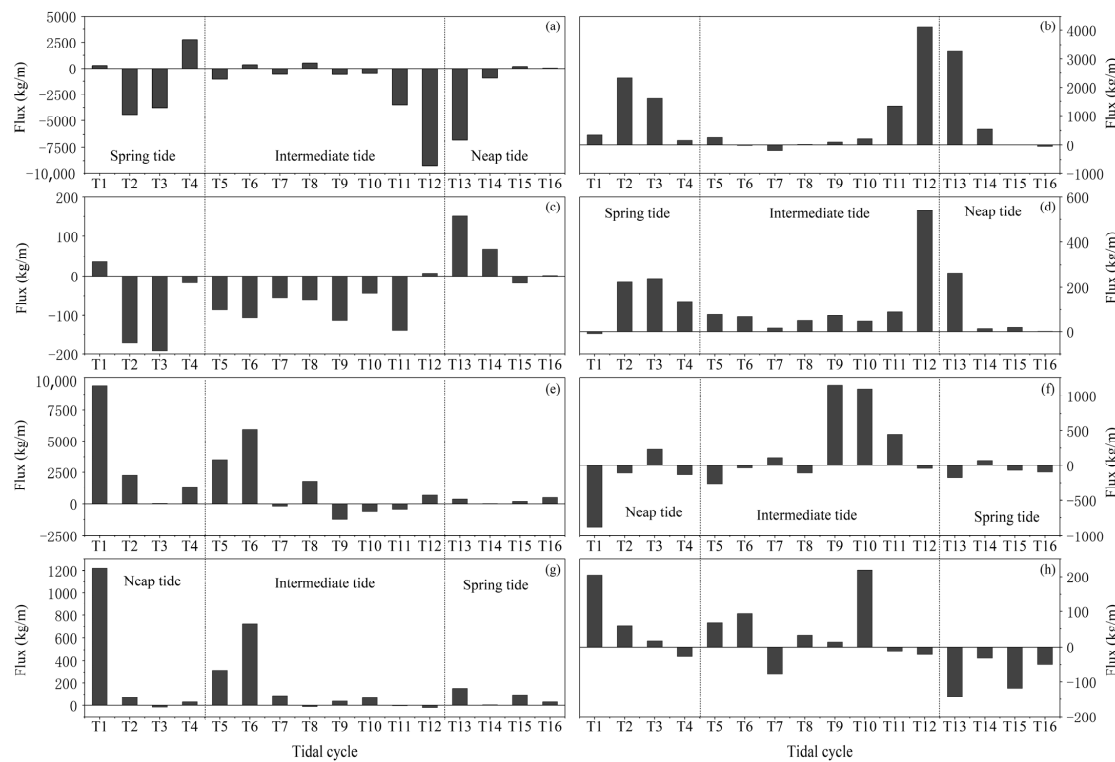


Figure 7. Transport flux of near-bed suspended sediment within a tidal cycle on the tidal flat in the study area: (a) northward and (b) eastward transport fluxes at B1 in winter; (c) northward and (d) eastward transport fluxes at B0 in winter; (e) northward and (f) eastward transport fluxes at B1 in summer; (g) northward and (h) eastward transport fluxes at B0 in summer.

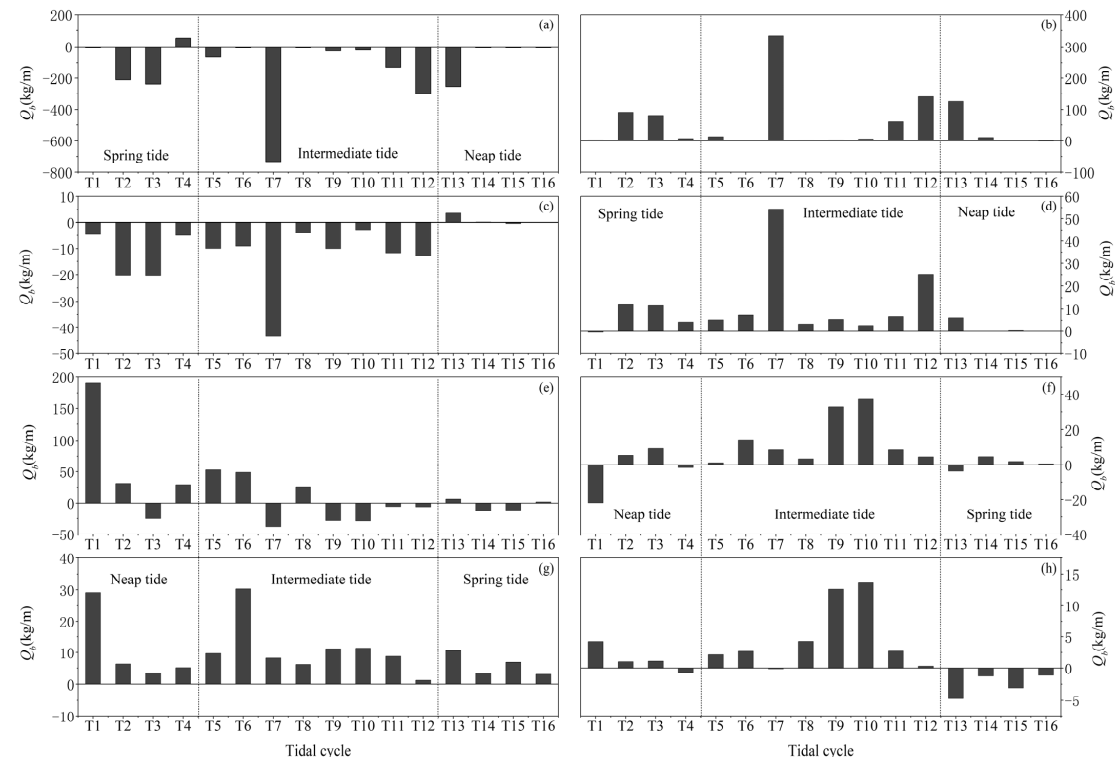


Figure 8. Bedload transport flux within a tidal cycle on the tidal flat in the study area: (a) northward and (b) eastward at B1 in winter; (c) northward and (d) eastward at B0 in winter; (e) northward and (f) eastward at B1 in summer; (g) northward and (h) eastward at B0 in summer.

Overall, as shown in Figure 9 and Table 3, the near-bottom suspended sediment and bedload in the tidal flat of the study area are mainly transported southeastward in winter and northward in summer, with the net transport fluxes being greater in the lower than in the upper intertidal flat; the net transport fluxes in the lower intertidal flat are greater in winter than in summer, while those in the upper intertidal flat are smaller in winter than in summer.

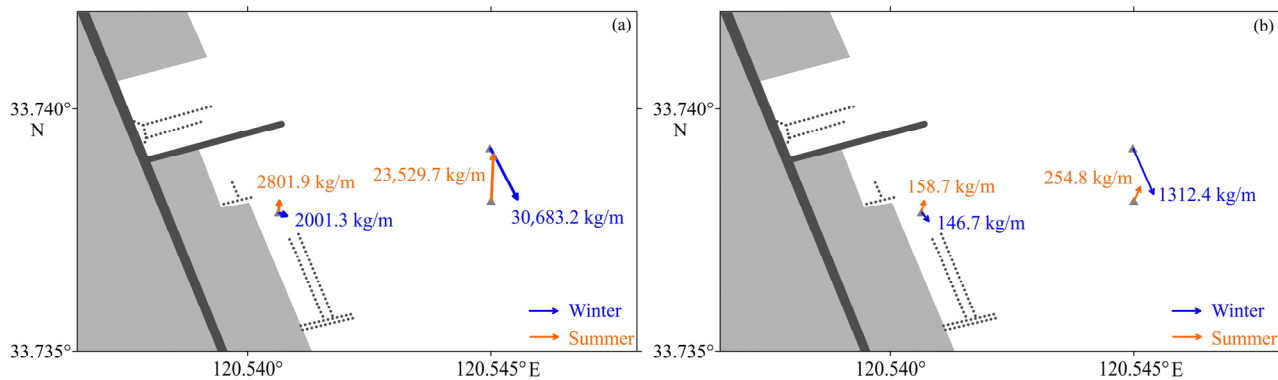


Figure 9. Net transport fluxes of (a) near-bed suspended sediment and (b) bedload on the tidal flat within a spring–neap tidal cycle in winter and summer.

Table 3. Total net erosion flux, net transport fluxes, and direction of near-bed suspended sediment and bedload within a spring–neap tidal cycle during the observation.

Station	Season	Net Erosion Flux (kg/m ²)	Net Transport of Near-Bed Suspended Sediment		Net Transport of Bedload	
			Flux (kg/m)	Direction (°)	Flux (kg/m)	Direction (°)
B0	Winter	−75.4	2001.3	111.5	146.7	140.1
	Summer	−83.0	2801.9	4.6	158.7	12.3
B1	Winter	−622.3	30,683.2	152.7	1312.4	156.3
	Summer	−516.5	23,529.7	2.9	254.8	24.6

5. Discussion

5.1. Spatiotemporal Variations in Tidal Flat Erosion–Accretion near the Sheyang River Estuary

The geomorphology and sediment composition of tidal flats are controlled by hydrodynamics, sediment supply, and biological activities [1]. The area corresponding to the tidal flat is gradually decreasing [3] due to sea-level rise, land subsidence, and intensifying human activities in river basins and coastal zones, of which human activities are the main driving factor [10] causing most tidal flats in the world to experience erosion [42–44]. Coastal erosion generally manifests as shoreline retreat and bed erosion [13,42]. Coastal erosion and accretion are fundamentally controlled by sediment balance at all spatiotemporal scales [45,46]. Since its diversion into the Yellow Sea in 1128, the Yellow River has brought a huge amount of sediment that has entered the Yellow Sea, providing sufficient fine-grained sediment for the development of tidal flats in the central and northern parts of the Jiangsu coast, which are rapidly accumulating [8]. However, the Yellow River shifted northward in 1855, cutting off the massive sediment supply and leading to erosion of the AYRD and adjacent coast zone. This erosion gradually decreases in intensity with an increase from the AYRD to the SYRE [8,13], while the tidal flat south of the SYRE exhibits accretion in the early period due to the southward transport of erosive sediments from the AYRD [14,15,47]. According to monitoring data from the China Marine Environmental Quality Bulletin, the proportion of eroded coastline length on the northern side of the SYRE increased from 58.4% in 2013 to 68.3% in 2017, while the average erosion rate decreased from 26.4 m/a to 10.5 m/a. Over time, the eroded coastline has continuously

moved southward, especially since 2000, when the coast south of the SYRE also gradually began to erode with progressive intensification of erosion [17–21]. Comparison of satellite images from different times shows that coastline erosion and destruction of aquaculture ponds have occurred in the study area and the adjacent coastline (approximately 4 km in length) since 2014, of which the rate of coastline retreat ranged from 12 m/a to 44 m/a during 2014–2019, with an average rate of 23.3 m/a, and the length of eroded coastline was 920 m. However, from 2019 to 2021, the coastline retreat rate increased rapidly from 13 m/a to 193 m/a, with an average rate of 43.5 m/a, and the length of eroded coastline increased to 3840 m, leading to the destruction of aquaculture ponds and rapid coastal retreat (Figure 10).

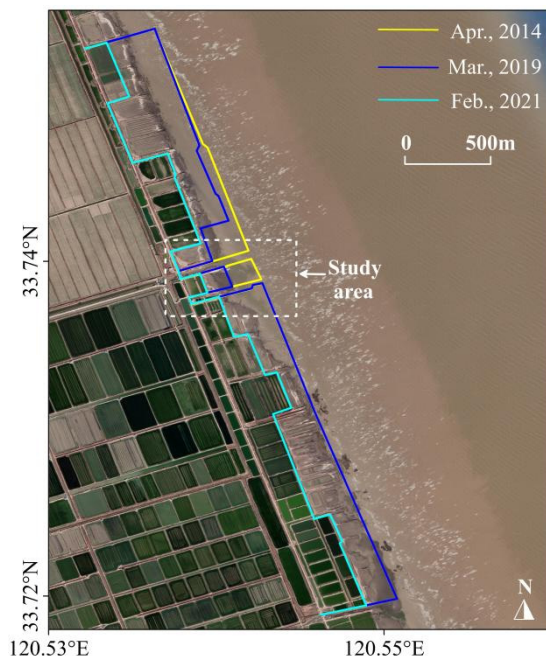


Figure 10. Coastline evolution from 2014 to 2021 near the study area.

Coastal erosion in central Jiangsu has been expanding, primarily due to changes in sediment sources and hydrodynamics. On the one hand, after the diversion of the Yellow River, the interruption of this massive sediment supply led to rapid erosion of the AYRD, and the eroded sediments were transported southward, thereby continuing to provide abundant sediment for the central Jiangsu tidal flats. However, with the implementation of coastal erosion protection projects, the sediment supply generated by coastal erosion gradually decreased, causing coastal erosion to extend southward [8,13,48]. The transitional area for erosion–accretion conversion in the central Jiangsu coast moved from the SYRE in the 1980s to the coast of the Xinyang River estuary (XYRE) and to Doulong River estuary (DLRE) [49]. On the other hand, due to the 20 km outward protrusion of the coastline of the AYRD and the magnificent subaqueous delta in the early period, the propagation of tidal waves from north to south were blocked, and with the retreat of the Jiangsu coastline, the subaqueous delta of the AYRD flattened, allowing tidal waves propagating from north to south to flow more smoothly, thereby enhancing the tidal flow on the southern side of the AYRD [50] and thus, intensifying the coastal erosion on the south side of the SYRE. Additionally, since 2000, there has been a rapid increase in projects of port construction and reclamation in the central Jiangsu coast [20], which has significantly impacted coastal erosion near the SYRE and its adjacent coastal area. Activities such as dredging of the Sheyang Port (SYP) navigation channels, construction of double guide levees in the SYP area, construction of sluices, and reclamation have influenced the hydrodynamic and erosion–accretion patterns near the SYRE, enhancing the coastal erosion near SYRE [51–53]. The observation and modeling results indicate that large-scale tidal flat

reclamation has altered the pattern of tidal energy distribution along the Jiangsu coast, resulting in strengthened M_2 tidal constituents [54] and leading to changes in sediment transport patterns and tidal flat geomorphology [25,55].

5.2. Mechanisms of Tidal Flat Erosion on the South Side of the Sheyang River Estuary

Sediment transport over intertidal flats is controlled by the combined action of tidal currents and waves. In the case of sufficient fine-grained sediment supply, suspended sediment and bedload are transported landward under the influences of “settling- and scour-lag effects” and “time-tidal current velocity asymmetry”, forming broad tidal flats [1,15,56], making it difficult for wave energy to penetrate into the intertidal area and resulting in significantly less wave-driven than tidal current-driven sediment transport [46]. However, when the supply of fine sediment is interrupted, the environment dominated by tidal action is disrupted, and the previously suppressed wave action gradually becomes active, with a gradual changing from accretion to erosion of tidal flats under the combined action of waves and tidal currents [46]. The observation results show that there is strong wave action in the intertidal flat of the study area under normal weather conditions. Although generally lower than τ_c , τ_w is significantly higher than τ_c during the early stage of flood tide, high tide, and the late stage of ebb tide (Figures 4 and 5). In terms of the average value of the tidal cycle, the proportion of $\tau_{cw} > \tau_{cr}$ in the lower intertidal flat during winter and summer is 84% and 82%, respectively, and 50% and 57%, respectively, in the upper intertidal flat, higher than the proportions observed in the tidal flats of the Yangtze River estuary [57]. The statistical results show that τ_w accounts for approximately 40% and 67% of τ_c in the lower and upper parts of intertidal flat, respectively, in winter, and the proportion was 46% and 66% in summer, respectively. This indicates that the tidal current has a larger contribution to tidal flat erosion in the lower intertidal flat on the south side of the SYRE, and the contribution of wave action is gradually increasing in the upper intertidal flat, which is consistent with the field observations and theoretical analyses [1,46,58].

Generally, tidal currents transport sediments landward when there is sufficient sediment supply, whereas wave action is more pronounced under conditions where sediment is transported seaward [1]. Based on the observed data, there is relatively strong wave action in the study area. Based on the calculated total net eastward transport fluxes of F_H and Q_b during a tidal cycle at B0 and B1, then from the perspective of sediment balance, we assume that if the net eastward transport flux across B1 is smaller than that across B0, it can be considered as a net input of sediment between the two stations; that is, deposition occurs on the tidal flat between two stations. On the contrary, if the net eastward transport flux across B1 is greater than that across B0, it can be considered as a net export of sediment between the two stations, that is, the erosion of the tidal flat between the two stations. The statistical results show that the total net eastward sediment load (e.g., $F_H + Q_b$) induced by τ_{cw} in the intertidal flat between B0 and B1 is 789.5 kg and 64.9 kg in winter and summer, respectively. In other words, a net export of sediment occurs between the two stations both in winter and in summer. Considering a wet sediment density of 1960 kg/m³ [59], the mean erosion depth of the intertidal flat area between the two stations throughout the year is calculated as 19.07 cm/a, which is less than the erosion depth near the AYRD (25 cm/a~33 cm/a) and more than that north of SYRE (13 cm/a~18 cm/a) [27]. It should be noted that for this net export flux of suspended sediment, only the transport fluxes of near-bed suspended sediment are considered and not the whole water column. Therefore, this calculation result may be affected by bed erosion intensity. According to the results calculated for erosion–deposition at two observation sites, both in winter and summer, there is much larger erosion flux than deposition flux in the intertidal flat of the study area, and the intertidal flat is dominated by net erosion (Figure 6). The net erosion depths induced by the combined action of waves and tidal currents in the lower and upper parts of the intertidal flat within a tidal cycle range from 0.37 cm to 3.96 cm and from 0 cm to 0.80 cm, respectively, with average erosion depths of 1.98 cm and 0.24 cm, respectively, in winter, and from 0.77 cm to 2.32 cm and from 0.06 cm to 0.61 cm, respectively, with average

erosion depths of 1.65 cm and 0.26 cm in summer, respectively. These erosion depths are greater than those observed in many tidal flats in the Yangtze River estuary, Yellow River estuary, Min River estuary, and North Sea [21,57,59–62], and the erosion rates are also higher than that of the tidal flats near XYRE in the southern part of the study area [63]. From Figure 9, it can be seen that both bedload and near-bed suspended sediment are transported southeast in winter and northeast in summer, and the total transport flux is greater in winter than in summer, indicating that throughout the year, there is net transport of the sediment from tidal flat erosion in this area southeast. The modeling results indicated that the sediment eroded by the tidal flats near the SYRE was mainly transported to the southeast and accumulated on the tidal flats near the Dafeng coastal area [25,26].

The calculated results show that there is a very high rate of bed erosion in the study area. One reason for this is that the tidal flats near the SYRE are currently experiencing severe erosion due to severe sediment supply deficiency [13], which results in an increase in bed slope [16,64], and the wave action strengthens, which then further aggravates the increase in the bed erosion rate. Another reason is due to limitations in the observation methods used in this paper. According to the instrument parameters and installation methods used in this study, the observation data are incorrect when the inundation height is less than 0.5 m. Therefore, the calculated fluxes of sediment transport and erosion–deposition in this study were obtained for periods when the submerged inundation height exceeded 0.5 m, which does not cover the entire tidal cycle, especially during the early stage of flood tide and late stage of ebb tide, when the inundation height is very shallow and wave action is more significant. The observation results also show that in extremely shallow-water environments (water depth less than 0.2 m), there are very evident variations in tidal flat erosion and accretion, with significant erosion caused by wave–current interaction during the early stage of flood tide [23] and substantial sediment deposition during the late stage of ebb tide [24], which were not included in this study. In addition, the intertidal flat is rich in algae and abundant in benthic biological activity, which significantly influences the critical shear stress for erosion of sediments [65,66]. In calculating the critical shear stress for erosion of surface sediments in this study, only sediment grain size composition was considered, and the factors of biological activity were not taken into account; thus, the actual critical shear stress for erosion may be underestimated. In summary, the erosion depth and erosion rate of the intertidal flat near the SYRE calculated in this study may be overestimated.

6. Conclusions

The tidal flats near the Sheyang River estuary in Jiangsu Province are currently experiencing severe erosion, and the erosion is intensifying, with constant migration of the eroded shoreline toward the south. The research findings of this study indicate the following:

(1) The surface sediments of the tidal flats on the southern side of the Sheyang River estuary are dominated by sand and silt, with the sediment being coarser in the lower intertidal flat than in the upper part. There are significantly stronger hydrodynamics in the lower than in the upper intertidal flat, and the variations in near-bed tidal current velocity show significant temporal characteristics on a seasonal scale, being larger in winter than in summer. There is no obvious seasonal variation of waves.

(2) The erosion processes on the south side of the Sheyang River estuary have evident spatiotemporal variation characteristics: the intertidal flat in the study area is in a state of erosion most of the time, with the higher erosion flux in the lower than in the upper intertidal flat; in the lower part of the intertidal zone, there is higher erosion flux in winter than in summer, while the opposite pattern is exhibited in the upper intertidal flat.

(3) Near-bed suspended sediment and bedload show net seaward transport in both the lower and upper parts of the intertidal flat, with net transport toward the southeast in winter and north-northeast in summer.

(4) The erosion of tidal flats on the south side of the Sheyang River estuary is characterized by coastline retreat and bed erosion. The average retreat rate of coastline in the

study area increased from 23.3 m/a during 2014–2019 to 43.5 m/a during 2019–2021, with the proportion of eroded coastline length increasing from 23% to 96%. The average erosion depth in the lower and upper parts of the intertidal flat with a tidal cycle is 1.98 cm and 0.24 cm, respectively, in winter and 1.65 cm and 0.26 cm in summer, respectively.

(5) The proportion of the wave-induced bottom shear stress to the tidal-current-induced bottom shear stress is 0.40~0.46 in the lower intertidal flat and increases to 0.66~0.67 in the upper intertidal flat, indicating that in the study area, intertidal flat erosion is primarily driven by tidal currents, with significant contributions from wave action, especially in the upper intertidal flat.

As a next step, we will improve our research methods, including by supplementing the observation and analysis of suspended sediment transport flux for the full water column and sedimentary dynamic processes in extremely shallow-water environments (<0.5 m) and studying the impact of biological activities on sediment erosion–deposition processes toward providing a clearer understanding of the erosion process and control mechanisms affecting tidal flats in the central Jiangsu coast.

Author Contributions: Conceptualization, W.Z., K.O., A.W. and X.Z.; data acquisition, W.Z., K.O., X.Z., A.W., Q.Y., X.Y. and C.Y.; data processing, W.Z., K.O., A.W. and Q.Y.; experiment: W.Z.; writing—original draft preparation, W.Z.; writing—review and editing, W.Z., K.O. and A.W.; funding acquisition, K.O. and X.Z. All authors have read and agreed to the published version of the manuscript.

Funding: This research was funded by the project sponsored by the Foundation of Observation and Research Station of East China Coastal Zone, MNR (No. ORSECCZ2022202) and the National Natural Science Foundation of China (No. U22A20585, 42076172).

Institutional Review Board Statement: Not applicable.

Informed Consent Statement: Not applicable.

Data Availability Statement: The original contributions presented in this study are included in the article. Further inquiries can be directed to the corresponding authors.

Conflicts of Interest: The authors declare no conflicts of interest.

References

1. Gao, S. Geomorphology and sedimentology of tidal flats. In *Coastal Wetlands: An Ecosystem Integrated Approach*, 2nd ed.; Perillo, G.M.E., Wolanski, E., Cahoon, D., Hopkinson, C., Eds.; Elsevier: Amsterdam, The Netherlands, 2019; pp. 359–381.
2. Eisma, D. *Intertidal Deposits: River Mouths, Tidal Flats, and Coastal Lagoons*; CRC Press: Boca Raton, FL, USA, 1997; p. 525.
3. Murray, N.J.; Phinn, S.R.; DeWitt, M.; Ferrari, R.; Johnston, R.; Lyons, M.B.; Clinton, N.; Thau, D.; Fuller, R.A. The global distribution and trajectory of tidal flats. *Nature* **2019**, *565*, 222–225. [[CrossRef](#)] [[PubMed](#)]
4. Reineck, H.-E.; Singh, I.B. *Depositional Sedimentary Environments*, 2nd ed.; Springer: Berlin/Heidelberg, Germany, 1980; p. 549.
5. Evans, G.; Collins, B.M. The transportation and deposition of suspended sediment over the intertidal flats of the Wash. In *Nearshore Sediment Dynamics and Sedimentation*; Hails, J., Carr, A., Eds.; John Wiley & Sons: Chichester, UK, 1975; pp. 273–306.
6. Amos, C.L.; Mosher, D.C. Erosion and deposition of fine-grained sediments from the Bay of Fundy. *Sedimentology* **1985**, *32*, 815–832. [[CrossRef](#)]
7. Wang, Y. The mudflat system of China. *Can. J. Fish. Aquat. Sci.* **1983**, *40* (Suppl. S1), 160–171. [[CrossRef](#)]
8. Ren, M.E. Tidal mud flat. In *Modern Sedimentation in the Coastal and Nearshore Zones of China*; Ren, M.E., Ed.; China Ocean Press: Beijing, China, 1986; p. 517. (In Chinese)
9. Schuerch, M.; Spencer, T.; Temmerman, S.; Kirwan, M.L.; Wolff, C.; Lincke, D.; McOwen, C.J.; Pickering, M.D.; Reef, R.; Vafeidis, A.T.; et al. Future response of global coastal wetlands to sea-level rise. *Nature* **2018**, *561*, 231–234. [[CrossRef](#)] [[PubMed](#)]
10. Li, X.; Bellerby, R.; Craft, C.; Widney, S.E. Coastal wetland loss, consequences, and challenges for restoration. *Anthr. Coasts* **2018**, *1*, 1–15. [[CrossRef](#)]
11. Walter, R.K.; O’Leary, J.K.; Vitousek, S.; Kitajima, A. Large-scale erosion driven by intertidal eelgrass loss in an estuarine environment. *Estuar. Coast. Shelf Sci.* **2020**, *243*, 106910. [[CrossRef](#)]
12. Hulskamp, R.; Luijendijk, A.; van Maren, B.; Moreno-Rodenas, A.; Calkoen, F.; Kras, E.; Lhermitte, S.; Aarninkhof, S. Global distribution and dynamics of muddy coasts. *Nat. Commun.* **2023**, *14*, 8259. [[CrossRef](#)] [[PubMed](#)]
13. Zhang, R.S.; Lu, L.Y.; Wang, Y.H. The mechanism and trend of coastal erosion of Jiangsu Province in China. *Geogr. Res.* **2002**, *21*, 469–478. (In Chinese with English abstract)

14. Zhu, D.K.; Xu, T.G. The coast development and exploit of middle Jiangsu. *J. Nanjing Univ. Nat. Sci. Ed.* **1982**, *18*, 799–818. (In Chinese with English abstract)
15. Gao, S.; Zhu, D.K. The profile of Jiangsu's mud coast. *J. Nanjing Univ. Nat. Sci. Ed.* **1988**, *24*, 75–84. (In Chinese with English abstract)
16. Chen, C.J. Development of depositional tidal flat in Jiangsu Province. *Oceanol. Limnol. Sin.* **1991**, *22*, 360–368. (In Chinese with English abstract)
17. Yan, Q.S.; Liu, R.J.; Ma, Y. Remote sensing analysis of shoreline changes along the coast near the Sheyang River Estuary of Jiangsu Province since 1973. *Mar. Sci.* **2015**, *39*, 94–100. (In Chinese with English abstract)
18. Cui, D.D.; Lyu, L.; Zhou, Y.; Deng, H.L.; Zhang, H.M.; Zhang, D.; Shen, Y.M. Remote sensing monitoring and preventive countermeasures of coastal erosion in Jiangsu Province. *Ocean. Dev. Manag.* **2021**, *38*, 84–89. (In Chinese with English abstract)
19. He, J.; Fu, C.L.; Shu, L.Y.; Zhang, G.; Wan, K.C. Analysis on the status quo and cause of erosion and deposition of Yancheng coastline in Jiangsu Province. *J. Geol.* **2021**, *45*, 189–196. (In Chinese with English abstract)
20. Huang, L.; Zhao, C.; Jiao, C.; Zheng, G.; Zhu, J. Quantitative Analysis of Rapid Siltation and Erosion Caused Coastline Evolution in the Coastal Mudflat Areas of Jiangsu. *Water* **2023**, *15*, 1679. [[CrossRef](#)]
21. Wang, K.; Li, H.; Zhang, N.; Zhang, J.; Zhang, X.; Gong, Z. Study on the Erosion and Deposition Changes of Tidal Flat in Jiangsu Province Using ICESat-2 and Sentinel-2 Data. *Remote Sens.* **2023**, *15*, 3598. [[CrossRef](#)]
22. Wang, A.J.; Ye, X. Erosion and deposition processes of cohesive sediment in *Spartina alterniflora* marsh, Luoyuan Bay in the north of Fujian coast, China. *Quat. Sci.* **2013**, *33*, 582–593. (In Chinese with English abstract)
23. Shi, B.W.; Cooper, J.R.; Li, J.S.; Yang, Y.; Yang, S.L.; Luo, F.; Yu, Z.X.; Wang, Y.P. Hydrodynamics, erosion and accretion of intertidal mudflats in extremely shallow waters. *J. Hydrol.* **2019**, *573*, 31–39. [[CrossRef](#)]
24. Chen, D.Z.; Tang, J.P.; Xing, F.; Cheng, J.; Li, M.L.; Zhang, Y.Y.; Shi, B.W.; Shi, L.Q.; Wang, Y.P. Erosion and accretion of salt marsh in extremely shallow water stages. *Front. Mar. Sci.* **2023**, *10*, 1198536. [[CrossRef](#)]
25. Xing, F.; Wang, Y.P.; Jia, J.J. Hydrodynamic and sediment transport patterns on intertidal flats along middle Jiangsu coast. *Anthropocene Coasts* **2022**, *5*, 12. [[CrossRef](#)]
26. Xing, F.; Wang, Y.P.; Wang, H.V. Tidal hydrodynamics and fine-grained sediment transport on the radial sand ridge system in the southern Yellow Sea. *Mar. Geol.* **2012**, *291*–294, 192–210. [[CrossRef](#)]
27. Wang, J. *Coastal Mudflat in Jiangsu Province and Their Utilization Potential*; China Ocean Press: Beijing, China, 2012; p. 564. (In Chinese)
28. Fugate, D.C.; Friedrichs, C.T. Determining concentration and fall velocity of estuarine particle populations using ADV, OBS and LISST. *Cont. Shelf Res.* **2002**, *22*, 1867–1886. [[CrossRef](#)]
29. Voulgaris, G.; Meyers, S.T. Temporal variability of hydrodynamics, sediment concentration and sediment settling velocity in a tidal creek. *Cont. Shelf Res.* **2004**, *24*, 1659–1683. [[CrossRef](#)]
30. Collins, M.B.; Ke, X.; Gao, S. Tidally-induced flow structure over intertidal flats. *Estuar. Coast. Shelf Sci.* **1998**, *46*, 233–250. [[CrossRef](#)]
31. Dyer, K.R. *Coastal and Estuarine Sediment Dynamics*; John Wiley & Sons: Chichester, UK, 1986; p. 341.
32. Pope, N.D.; Widdows, J.; Brinsley, M.D. Estimation of bed shear stress using the turbulent kinetic energy approach-A comparison of annular flume and field data. *Cont. Shelf Res.* **2006**, *26*, 959–970. [[CrossRef](#)]
33. Soulsby, R. *Dynamics of Marine Sands: A Manual for Practical Applications*; Thomas Telford: London, UK, 1997; p. 249.
34. Longuet-Higgins, M.S. On the statistical distribution of the height of sea waves. *J. Mar. Res.* **1952**, *11*, 245–266.
35. Karimpour, A.; Chen, Q. Wind wave analysis in depth limited water using OCEANLYZ, A MATLAB toolbox. *Comput. Geosci.* **2017**, *106*, 181–189. [[CrossRef](#)]
36. Fredsoe, J.; Deigaard, R. *Mechanics of Coastal Sediment Transport*; World Scientific: Singapore, 1992; p. 369.
37. Krone, R.B. Flume studies of the transport of sediment in estuarine shoaling processes. In *Final Report to San Francisco District*; U.S. Army Corps of Engineers: Washington, DC, USA, 1962.
38. Partheniades, E. Erosion and deposition of cohesive soils. *J. Hydraul. Div. Proc. ASCE* **1965**, *91*, 105–139. [[CrossRef](#)]
39. Robert, W.; Whitehouse, R.J.S. Predicting the profile of intertidal mudflats formed by crossshore tidal currents. In *Coastal and Estuarine Fine Sediment Processes*; McAnally, W.H., Mehta, A.J., Eds.; Elsevier Science: Amsterdam, The Netherlands, 2001; pp. 263–285.
40. Whitehouse, R.J.S.; Soulsby, R.L.; Roberts, W.; Mitchener, H.J. *Dynamics of Estuarine Muds: A Manual for Practical Applications*; Thomas Telford: London, UK, 2000; pp. 42–186.
41. Bagnold, R.A. Mechanics of marine sedimentation. In *The Sea: Ideas and Observations*; Hill, M.N., Ed.; Wiley-Interscience: New York, NY, USA, 1963; pp. 507–528.
42. Cai, F.; Su, X.Z.; Liu, J.H.; Li, B.; Lei, G. Coastal erosion in China under the condition of global climate change and measures for its prevention. *Prog. Nat. Sci.* **2009**, *19*, 415–426. [[CrossRef](#)]
43. Fan, D.D. Open-Coast Tidal Flats. In *Principles of Tidal Sedimentology*; Davis, R.A., Dalrymple, R.W., Eds.; Springer Science: New York, NY, USA, 2012; pp. 187–229.
44. Zhong, Z.; Hu, Z. The Impact of Reclamation on Tidal Flat Morphological Equilibrium. *Front. Mar. Sci.* **2021**, *8*, 769077. [[CrossRef](#)]
45. Woodroffe, C.D. *Coasts: Form, Process and Evolution*; Cambridge University Press: Cambridge, UK, 2002; p. 620.

46. Gao, S.; Jia, J.J.; Yu, Q. Theoretical framework for coastal accretion-erosion analysis: Material budgeting, profile morphology, shoreline change. *Mar. Geol. Quat. Geol.* **2023**, *43*, 1–17. (In Chinese with English abstract)
47. Jiang, B.X. Dynamic status of erosion and deposition along Yancheng Coast, Jiangsu Province. *Acta Oceanol. Sin.* **1993**, *15*, 57–62. (In Chinese)
48. Yu, Z.Y.; Chen, D.C.; Jin, L. The formation and erosion transformation of the old Yellow River subaqueous delta in northern Jiangsu province. *Acta Oceanol. Sin.* **1986**, *8*, 197–206. (In Chinese)
49. Chen, W.T.; Zhang, D.; Shi, S.J.; Zhou, J.; Kang, M. Research on monitoring coastline changes by remote sensing in muddy coast, central Jiangsu coast. *Haiyang Xuebao* **2017**, *39*, 138–148. (In Chinese with English abstract)
50. Chen, K.F.; Wang, Y.H.; Lu, P.D.; Yu, L.L. Research on the abandoned Huanghe River Delta erosion process and impact on tidal current characteristics of the Huanghai Sea off the coast of North Jiangsu, China. *Acta Oceanol. Sin.* **2013**, *35*, 189–196. (In Chinese with English abstract)
51. He, X.Y.; Wang, Y.P.; Zhu, Q.G.; Zhang, Y.; Zhang, D.; Zhang, J.C.; Yang, Y.; Gao, J.H. Simulation of sedimentary dynamics in a small-scale estuary: The role of human activities. *Environ. Earth Sci.* **2015**, *74*, 869–878. [[CrossRef](#)]
52. Liu, Q.; Zhang, G.; Xiang, L.H.; Zhang, X.F. Characteristics and genesis of erosion and deposition in Sheyang Port before and after double-dyke construction. *Mar. Sci. Bull.* **2017**, *36*, 561–567. (In Chinese with English abstract)
53. Li, M.L.; Wu, S.L.; Gong, X.L.; Yang, L.; Gou, F.G.; Li, J. Characteristics of coastline change under the influence of human activities in central Jiangsu Province from 1989 to 2019. *Mar. Sci.* **2022**, *46*, 60–68. (In Chinese with English abstract)
54. Lim, B.J.; Chang, Y.S.; Cho, Y.K. Effects of stepwise tidal flat reclamation on tidal evolution in the East China and Yellow Sea. *Environ. Res. Lett.* **2023**, *18*, 104041. [[CrossRef](#)]
55. Wang, Y.P.; Gao, S.; Jia, J.J.; Thompson, C.E.L.; Gao, J.H.; Yang, Y. Sediment transport over an accretional intertidal flat with influence of reclamation, Jiangsu coast, China. *Mar. Geol.* **2012**, *291–294*, 147–161. [[CrossRef](#)]
56. Postma, H. Transport and accumulation of suspended matter in the Dutch Wadden Sea. *Neth. J. Sea Res.* **1961**, *1*, 148–190. [[CrossRef](#)]
57. Shi, B.W.; Yang, S.L.; Wang, Y.P.; Bouma, T.J.; Zhu, Q. Relating accretion and erosion at an exposed tidal wetland to the bottom shear stress of combined current-wave action. *Geomorphology* **2012**, *138*, 380–389. [[CrossRef](#)]
58. Colosimo, I.; de Vet, P.L.M.; van Maren, D.S.; Reniers, A.J.H.M.; Winterwerp, J.C.; van Prooijen, B.C. The impact of wind on flow and sediment transport over intertidal flats. *J. Mar. Sci. Eng.* **2020**, *8*, 910. [[CrossRef](#)]
59. Jia, Y.G.; Zheng, J.W.; Yue, Z.; Liu, X.L.; Shan, H.X. Tidal flat erosion of the Huanghe River Delta due to local changes in hydrodynamic conditions. *Acta Oceanol. Sin.* **2014**, *33*, 116–124. [[CrossRef](#)]
60. Hu, Z.; Yao, P.; van der Wal, D.; Bouma, T.J. Patterns and drivers of daily bed level dynamics on two tidal flats with contrasting wave exposure. *Sci. Rep.* **2017**, *7*, 7088. [[CrossRef](#)]
61. Belliard, J.P.; Silinski, A.; Meire, D.; Kolokythas, G.; Levy, Y.; Van Braeckel, A.; Bouma, T.J.; Temmerman, S. High-resolution bed level changes in relation to tidal and wave forcing on a narrow fringing macrotidal flat: Bridging intra-tidal, daily and seasonal sediment dynamics. *Mar. Geol.* **2019**, *412*, 123–138. [[CrossRef](#)]
62. Xie, W.; Sun, J.; Guo, L.; Xu, F.; Wang, X.; Ji, H.; Fan, Y.; Wang, Z.B.; He, Q. Distinctive sedimentary processes on two contrasting tidal flats of the Yellow River Delta. *Front. Mar. Sci.* **2023**, *10*, 1259081. [[CrossRef](#)]
63. Zhao, Y.Y.; Yu, Q.; Wang, D.D.; Wang, Y.P.; Wang, Y.W.; Gao, S. Rapid formation of marsh-edge cliffs, Jiangsu coast, China. *Mar. Geol.* **2017**, *385*, 260–273. [[CrossRef](#)]
64. Yu, K.; Tao, J.F.; Zhou, Z.Y.; Aarninkhof, S.; Wang, Z.B. Sediment characteristics and intertidal beach slopes along the Jiangsu coast, China. *J. Mar. Sci. Eng.* **2021**, *9*, 347. [[CrossRef](#)]
65. Paarlberg, A.J.; Knaapen, M.A.F.; de Vries, M.B.; Hulscher, S.J.M.H.; Wang, Z.B. Biological influences on morphology and bed composition of an intertidal flat. *Estuar. Coast. Shelf Sci.* **2005**, *64*, 577–590. [[CrossRef](#)]
66. Shi, B.W.; Pratolongo, P.D.; Du, Y.F.; Li, J.S.; Yang, S.L.; Wu, J.H.; Xu, K.H.; Wang, Y.P. Influence of macrobenthos (*Meretrix meretrix Linnaeus*) on erosion-accretion processes in intertidal flats: A case study from a cultivation zone. *J. Geophys. Res. Biogeosciences* **2020**, *125*, e2019JG005345. [[CrossRef](#)]

Disclaimer/Publisher’s Note: The statements, opinions and data contained in all publications are solely those of the individual author(s) and contributor(s) and not of MDPI and/or the editor(s). MDPI and/or the editor(s) disclaim responsibility for any injury to people or property resulting from any ideas, methods, instructions or products referred to in the content.